JMEPEG (2012) 21:1562–1579
DOI: 10.1007/s11665-011-0065-3

1059-9495/$19.00

Potential Improvements in Shock-Mitigation Efficacy of a Polyurea-Augmented Advanced Combat Helmet

A. Grujicic, M. LaBerge, M. Grujicic, B. Pandurangan, J. Runt, J. Tarter, and G. Dillon

(Submitted October 6, 2011)

The design of the currently used Advanced Combat Helmet (ACH) has been optimized to attain maximum protection against ballistic impacts (fragments, shrapnel, etc.) and hard-surface collisions. However, the ability of the ACH to protect soldiers against blast loading appears not to be as effective. Polyurea, a micro-segregated elastomeric copolymer has shown superior shock-mitigation capabilities. In the present work, a combined Eulerian/Lagrangian transient non-linear dynamics computational fluid/solid interaction analysis is used to investigate potential shock-mitigation benefits which may result from different polyurea-based design augmentations of the ACH. Specific augmentations include replacement of the currently used suspension-pad material with polyurea and the introduction of a thin polyurea internal lining/external coating to the ACH shell. Effectiveness of different ACH designs was quantified by: (a) establishing the main forms of mild traumatic brain injury (mTBI); (b) identifying the key mechanical causes for these injuries; and (c) quantifying the extents of reductions in the magnitude of these mechanical causes. The results obtained show that while the ACH with a 2-mm-thick polyurea internal lining displays the best blast mitigation performance, it does not provide sufficient protection against mTBI.

Keywords Advanced Combat Helmet, internal lining/external coating, traumatic brain injury

1. Introduction

The work described in the present manuscript deals with the use of computational methods and tools to examine the shock-mitigation efficacy (critical from the standpoint of reducing the potential for traumatic brain injury (TBI) during exposure to blast loading) of polyurea when this elastomeric material is utilized in the construction of different components of the Advanced Combat Helmet (ACH). Hence, the key aspects of the present work are: (a) TBI; (b) ACH design; and (c) polyurea. These aspects will be briefly overviewed in the remainder of this section.

1.1 Traumatic Brain Injury

According to the Defense and Veterans Brain Injury Center (DVBIC) more than 150,000 US military personnel have been medically diagnosed with TBI since 2001 (Ref 1). Examination of these injuries revealed that ca. 2% could be attributed to skull penetration/fracture, ca. 89% could be classified as non-skull penetration/non-fracture brain injuries while the remaining 9% could not be readily classified (Ref 2). Among the non-skull penetration/non-fracture brain injuries diagnosed in soldiers returning from Afghanistan and Iraq, 46.7 and 63.9% were attributed to the soldier's exposure to blasts, respectively (Ref 3). The remaining non-skull penetration/non-fracture brain injuries could be attributed to blunt impacts, burns, etc. (Ref 4). This summary along with the associated high direct and indirect economic costs to society at large (through lost earning potential of the affected and the burden of care imposed on their families) and life-altering long-term consequences to the affected personnel shows that non-skull penetration/non-fracture brain injuries resulting from the soldier's exposure to blast are important problems that need an urgent solution. It is interesting to note that as advanced body armor and head protection gear have greatly reduced soldier fatalities from explosion and ballistic attacks, the problem of brain injuries in the attack survivors has become more prevalent (Ref 5-7). In particular, the problem of blast-induced brain injuries, which are typically not accompanied by visible, external bodily injuries, have become a serious problem. The present study will address some aspects of these brain injuries, referred to in the remainder of this manuscript as blast-induced TBIs.

Blast-induced TBIs are classified in a number of ways. One of these classifications identifies: penetrating (pTBIs) and closed (cTBIs) where the former involves skull penetration/fracture while, in the latter case, structural integrity of the skull is maintained. As mentioned above, the present investigation deals with cTBIs.

Closed TBIs can be further classified according to the severity-level as (Ref 8): (a) mild (mTBIs, also referred to as "concussions"); (b) moderate; and (c) severe. In the present work, the attention is focused on closed mTBIs.

Furthermore, according to the origin of TBI—causing dynamic loading, closed mTBIs can be classified as: (a) primary TBI resulting from the propagation and reflection of

A. Grujicic and **M. LaBerge**, Department of Bioengineering, Clemson University, Clemson, SC 29634; **M. Grujicic** and **B. Pandurangan**, Department of Mechanical Engineering, Clemson University, 241 Engineering Innovation Building, Clemson, SC 29634-0921; **J. Runt**, Department of Material Science and Engineering, Pennsylvania State University, University Park, PA 16082; and **J. Tarter** and **G. Dillon**, Applied Research Laboratories, Pennsylvania State University, University Park, PA 16082. Contact e-mail: gmica@clemson.edu.

shock waves (within the intracranial cavity) produced directly by the blast; (b) secondary TBI caused by the ballistic impact of a person's head with an object propelled by the blast; (c) tertiary TBI caused by the blast-induced propulsion of a person's head and its subsequent impact against a rigid/hard surrounding structure; and (d) quaternary TBI caused by heat, electromagnetic pulses, or toxic byproducts (Ref 6, 9). The present work deals with closed, primary, mTBIs.

Closed, primary, mTBIs can be further classified based on the nature of the injury as: (a) diffuse axonal injury; (b) contusion; and (c) subdural hemorrhage (Ref 10). Details regarding these types of mTBIs will be presented later in the manuscript.

1.2 ACH Design

Helmet has been traditionally used as the main head protection gear in the military. However, the design of military helmets has continuously evolved to respond to ever-increasing lethality and diversity of threats, to take advantage of the new materials and fabrication/manufacturing technologies, and to meet continuously growing demands for lower weight and improved comfort. An overview of the evolution/advances in the helmet design from one used in World War I to the ones currently in use can be found in Ref 11. Currently, two helmet designs are mainly being used by the US military (Ref 12): (a) the so-called Advanced Combat Helmet (ACH); and (b) the so-called Light-weight Marine Corps Helmet (LWH). The present work deals with the ACH design (described below), while a fairly detailed description of the LWH design (not considered here) can be found in our recent work (Ref 13).

An ACH helmet consists of a 7.8-mm-thick outer composite shell based on lower-content phenolic resin reinforced with higher-strength Kevlar® 129 fibers, a modified edge cut for lower protection surface and a "suspension system" (a set of discrete foam pads strategically placed on the interior surface of the helmet and held in place by Velcro-based hook-and-loop fasteners). A geometrical model of the ACH helmet, with all its basic components identified, is displayed in Fig. 1. To protect their intellectual property and maintain an advantage over their competitors, the helmet manufacturers have not revealed much detail regarding the material selection, fabrication methods and

Fig. 1 The Advanced Combat Helmet (ACH): (a) external side view; (b) suspension system side view; and (c) suspension system bottom view

designs of the suspension pads. What is known for sure is that the suspension pads are made of an elastomeric foam-like material (referred to as "Army foam") their geometrical dimensions and their locations in the helmet. A survey of the usage of foam-like materials carried out as part of the present work suggested that Ethylene Vinyl Acetate (EVA) foam is a good suspension-pad material candidate. Hence, EVA was used as the standard suspension-pad material in the present work.

1.3 Polyurea

Polyurea falls into a class of microphase-segregated and thermoplastically cross-linked elastomeric copolymers (the terms 'microphase-segregated' and 'thermoplastically cross-linked' will be defined later) that are formed by the rapid chemical reaction between isocyanates (organic chemicals containing isocyanate -N=C=O groups) and amines (organic chemicals containing amine -NH_2 groups). There are two aspects of this material which are often cited as being particularly attractive: (a) the copolymerization/gel reaction times are typically less than a minute so that this material can be produced using a spraying process; and (b) a variety of microstructures can be obtained through small variations in the chemistry and/or synthesis conditions. Examination of the structure of polyurea molecules/chains shows the presence of urea linkages (-NH-CO-NH-) which are polar (i.e., contain centers/poles of negative and positive charge) and together with the adjoining di-phenyl methane (C_6H_5-CH_2-C_6H_5) functional groups form the so-called "hard (i.e., high-stiffness) segments". Within the same molecule, various aliphatic functional groups form the so-called "soft (i.e., low stiffness) segments". As a result of strong hydrogen bonding between urea linkages of the neighboring chains (or the neighboring portions of the same chain), hard segments are typically micro-phase segregated into the so-called nanometer-sized "hard (i.e., high glass-transition temperature, often crystallized) domains". The non-segregated hard segments and the soft segments form the so-called "soft (i.e., low glass-transition temperature, amorphous) matrix". Due to the presence of (hard domain + soft matrix) two-phase structure, polyurea is often referred to as being "segmented". Furthermore, since strong hydrogen bonding within the hard domains provides inter-molecular joining, polyureas are often referred to as being thermoplastically cross-linked (in contrast to more commonly observed covalently cross-linked) polymers. An example of a prototypical polyurea microstructure as revealed using the atomic force microscope (AFM) tapping mode is depicted in Fig. 2. Examination of this figure suggests that polyurea should be treated as a nano-composite (in which hard domains act not only as thermoplastic cross-links but also as rigid reinforcements within a continuous soft matrix) rather than a homologous amorphous material.

Due to their highly complex internal microstructure described above, polyureas display a very broad range of mechanical responses under static and dynamic loading conditions. The main features of these responses can be defined as (e.g., Ref 14-16): (a) a high-level of stress versus strain constitutive non-linearity; (b) extreme strain-rate (and temperature) sensitivity; and (c) a high degree of pressure dependence. These types of mechanical responses have favored the use of polyurea as an abrasion/corrosion protection and blast/ballistic-impact mitigation material (e.g., Ref 17-19). For instance, polyureas are frequently used as:

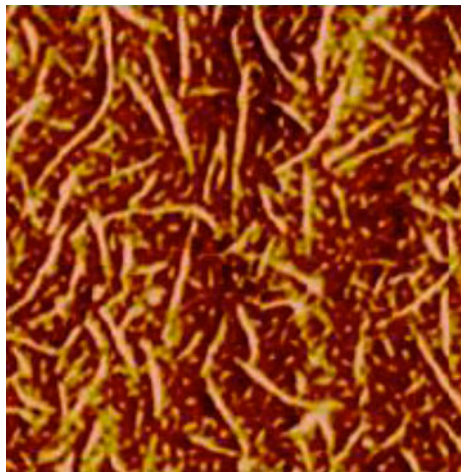

Fig. 2 A typical tapping-mode AFM phase image of polyurea showing its micro-segregated structure consisting of ribbon-like hard domains and a soft matrix

(a) Tough, abrasion-resistant, corrosion-resistant, durable, and impact-resistant (epoxy/rubber replacement) spray-on coatings/liners in various construction/structural applications such as tunnels, bridges, roofs, parking decks, storage tanks, freight ships, truck beds, etc.;
(b) External and internal wall-sidings and foundation coatings for buildings aimed at minimizing the degree of structure fragmentation and, in turn, minimizing the extent of the associated collateral damage in the case of a bomb blast; and
(c) Gun-fire/ballistic resistant and explosion/blast mitigating coatings/liners or inter-layers in blast-resistant sandwich panels for military vehicles and structures.

The applications mentioned above capitalize on the exceptional ability of polyureas to harden under applied loading and to alter/disperse shock waves and absorb the kinetic energy associated with these waves/ballistic projectiles (under dynamic loading conditions) (Ref 6, 7, 16).

1.4 Main Objective

The main objective of the present work is to assess the ability of polyurea, when used within the ACH (either as a suspension-pad material, composite-shell internal lining, or composite-shell external coating), to mitigate the effects of blast loading and, in turn, to reduce the possibility of the occurrence/probability of mild, primary, closed TBI.

1.5 Organization of the Paper

A brief description of a typical transient non-linear dynamics problem such as the one dealing with the interactions of an airborne blast wave with the human head protected by the ACH is given in section 2.1. Detailed descriptions of the geometrical and meshed models for the air/ACH/head assembly are presented in section 2.2. A fairly detailed account of the material models assigned to air and the different sections of the ACH/head assembly is provided in section 2.3. Formulation of the problem dealing with the interactions of an airborne blast wave with the ACH/head assembly is presented in section 2.4. The results obtained in the present work are presented and

discussed in section 3. The main conclusions resulting from the present work are summarized in section 4.

2. Modeling and Computational Procedure

2.1 Transient Non-linear Dynamics Analysis of Blast Loading of ACH/Head Assembly

A typical transient non-linear dynamics problem such as the interactions between an airborne blast wave and a human-head protected by an ACH involves solving simultaneously the governing partial differential equations for the conservation of momentum, mass, and energy along with the material constitutive equations and the equations defining the initial, boundary, kinematic constraint, and contact conditions. The aforementioned equations are typically cast within a coupled Eulerian/Lagrangian formulation and solved numerically using a second-order accurate explicit scheme, i.e., due to the large motions and deformations experienced by air, it is more computationally efficient to analyze the air-region using an Euler control-volume computational scheme (the computational grid is fixed in space and time while the air moves through it). On the other hand, the ACH/head assembly which undergoes considerably less motion and deformation is analyzed using a Lagrange scheme (the computational grid is tied to the materials constituting the ACH/head assembly and moves and deforms with it).

All the calculations carried out in this work were done using ABAQUS/Explicit, a general-purpose transient non-linear dynamics analysis software (Ref 20). The interactions (including self-interactions) or bonding between different components of the model are analyzed using the appropriate Lagrange-Lagrange and Euler-Lagrange contact/sliding and kinematic coupling options. For example, Lagrange-Lagrange interactions are analyzed in ABAQUS/Explicit using a "penalty" contact method within which the penetration of the surfaces into each other is resisted by linear spring forces/contact pressures with values proportional to the depth of penetration. These forces, hence, tend to pull the surfaces into an equilibrium position with no penetration. Contact pressures between two Lagrangian bodies are not transmitted unless the nodes on the "slave surface" of one body contact the "master surface" of the other body. There is no limit to the magnitude of the contact pressure that could be transmitted when the surfaces are in contact. Transmission of shear stresses across the contact interfaces is defined in terms of a static and a kinetic friction coefficient as well as an upper-bound shear stress limit (a maximum value of shear stress which can be transmitted before the contacting surfaces begin to slide).

Interactions between an Eulerian region (containing air and a propagating blast wave) and a Lagrangian region (containing the ACH/head assembly) are treated as a fluid/solid interaction problem. In these types of problems, the Lagrangian-type solid structures' free surfaces define the inner/contact boundaries for the Eulerian region (i.e., the Lagrangian region resides fully or partially within the Eulerian region and provides "no-flow" boundary conditions to the fluid in the direction of the local surface normal) while the Eulerian region provides surface traction boundary conditions to the Lagrangian region.

2.2 Geometrical and Meshed Models

Two distinct geometrical/mesh models are used in the present work: (a) a simple cube-shaped Eulerian-domain model was used to represent the ambient air and a single planar blast wave traveling through it; and (b) a Lagrangian-domain model for the complete ACH/head assembly, placed within the Eulerian domain. The two models are described in greater detail below.

2.2.1 Eulerian Domain. This cube-shaped domain with an edge length of 400 mm was meshed using eight-node cubic elements with an average edge length of 7 mm. Thus, the domain contains approximately 185,000 elements/cells, not including those elements occupied by the Lagrangian helmet/head assembly. Due to the Eulerian nature of the domain, the cells are not distorted/deformed during the analysis of blast wave/helmet/head assembly interactions. However, in order to capture the hydrodynamic fields in the regions adjacent to the blast wave front with higher resolution, an adaptive meshing algorithm was used which effectively attaches the mesh to the advancing blast wave. The Eulerian domain is filled with air. Details regarding the material model for air are presented in the next section.

2.2.2 Lagrangian Domain. The CAD model of the head developed in our previous work (Ref 13) was augmented to include the skin/fat external tissue, combined with the ACH CAD model developed by www.turbosquid.com and meshed/preprocessed for the ABAQUS/Explicit finite element program (Ref 20) using the general purpose pre-processing program HyperMesh from Altair, Inc. (Ref 21). The head model includes the following seven sections: main brain (*cerebrum*), cerebrospinal fluid (CSF, *liquor cerebrospinalis*), small brain (*cerebellum*), brain stem (*truncus encephali*), pituitary gland (*glandula pituitaria*), the skull (*cranium*), and skin/fat tissue. These components are depicted in Fig. 3. ACH model, in its base-line configuration consists of an outer composite shell, seven suspension pads, and a restraint system. In addition, in its augmented configuration, the ACH contains either a (2 mm thick) internal lining or a (2 mm thick) external coating.

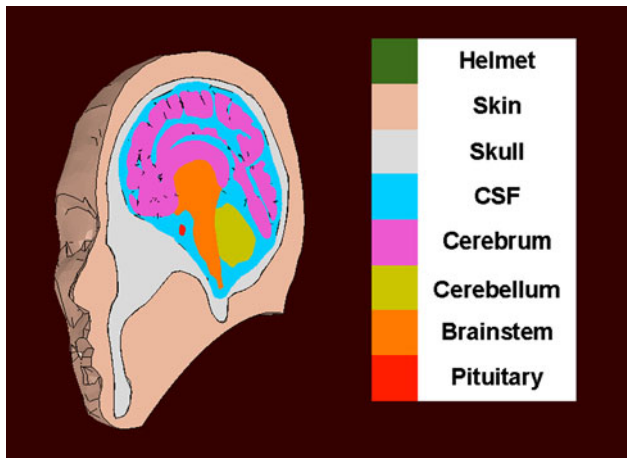

Fig. 3 Sagittal section of the human head model (with all the components properly labeled) used in the present work

The aforementioned ACH components are depicted in Fig. 4. In Fig. 5(a) and (b), the cube-shaped Eulerian and the Lagrangian domains are displayed for the cases of an unprotected head and an ACH-protected head, respectively. For clarity, the Eulerian air domain is made transparent. It should be pointed out that the standard bioengineering coordinate system was used in the present work (i.e., the finite element model of the skull/brain assembly is oriented in such a way that the positive x-axis is pointing forward, y-axis upward, and z-axis from left to right).

The finite element model of the ACH/head assembly (with 240 mm × 265 mm × 245 mm overall maximum dimensions along the three coordinate axes used in the present work) consists of approximately 550,000 (in the case of unprotected head) to 700,000 (in the case of the augmented ACH) first-order tetrahedral solid finite elements with a typical element edge length of 2 mm. This Lagrangian mesh size was found to be a good compromise between accuracy and computational efficiency. The use of finer meshes was found to produce somewhat different numerical values of the key field quantities. However, they did not alter the nature of the basic findings obtained in the present work. Typical head and ACH finite element meshes used in the present work are displayed in Fig. 3 and 4, respectively. Connections between adjacent head sections were established by having them share nodes along adjoining interfaces while contact surfaces are created between the suspension pads and the skull/composite shell.

The next section identifies the materials used in the ACH/head assembly as well as in the surrounding ambient atmosphere and presents their constitutive models suitable for use under blast-induced high deformation rate conditions.

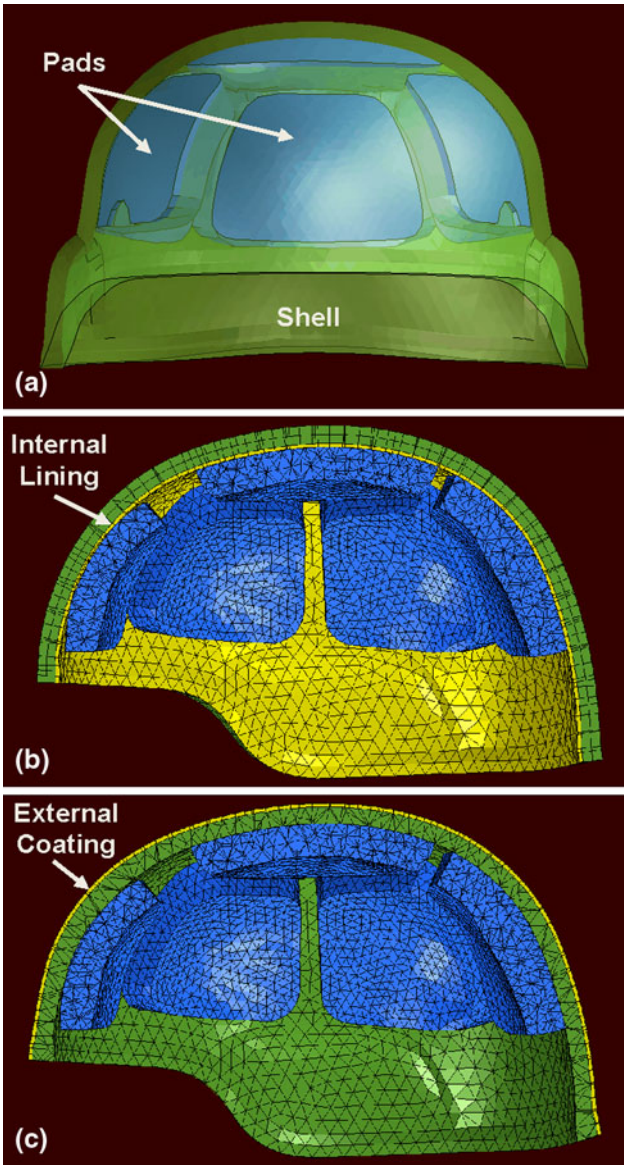

Fig. 4 (a) Geometrical model of the ACH in its standard configuration (helmet shell is made transparent for clarity); (b, c) sagittal cut meshed models for the augmented ACH with an internal lining and an external coating, respectively

2.3 Material Models

The material (mechanical) models of interest here, define relationships between the field/material-state variables (pressure/stress, mass-density/specific volume, energy-density, temperature, etc.). These relations are typically defined as: (a) an equation of state; (b) a strength model; and (c) a failure model. Partitioning of the material model in these three components is a natural consequence of the fact that, the total stress tensor can be represented as a sum of a hydrostatic stress (scales with

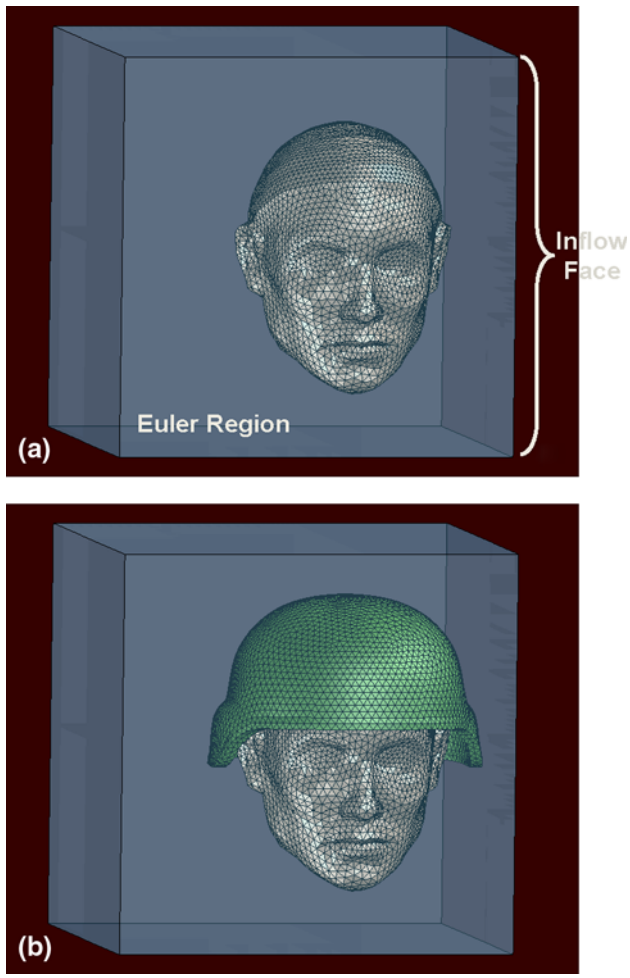

Fig. 5 The Eulerian/Lagrangian domain assembly used for the cases of (a) an unprotected head; and (b) a ACH-protected head

negative pressure) tensor (which causes a change in the volume/density of the material) and a deviatoric stress tensor (which is responsible for the shape change of the material). The hydrostatic part of the stress is defined by the equation of state which specifies the corresponding functional relationship between pressure, mass-density, and internal-energy density/temperature. The deviatoric part of the stress, on the other hand, is defined by the strength model which specifies the appropriate functional relations between the deviatoric-stress components and various field quantities quantifying the extent and rate of material deformation as well as the effect of material temperature. A failure model, defines one or more stress-and/or strain-based conditions, which when attained, cause the material to fracture and lose its ability to support tensile normal and shear stresses. Due to the fact that blast levels considered in the present work typically do not cause any detectable damage to the helmet, skull, or the inter-cranial brain matter and due to the (non-fracturable) fluid nature of air, failure of the materials encountered in the present problem was not considered. Furthermore, since blast loading scenarios considered in the present work are not generally associated with significant thermal-radiation effects or energy-dissipation induced heat effects (i.e., the shock loading conditions fall into the weak-shock regime), the effect of temperature on the material response/behavior was not considered.

As discussed earlier, the present work deals with interactions between an airborne blast wave and the ACH/head assembly. Since these interactions result in the formation of the shock waves (in the case of the so-called "normal materials") or finite-amplitude spreading waves (in the case of the so-called "anomalous materials"), within the ACH/head assembly, special attention was paid to the ability of the material models used in the present work to enable formation of the blast/induced waves of the correct type. Specifically, as discussed in our prior work (Ref 13): (a) shock-supporting normal materials must display material non-linearity of a type which yields an upward curvature in the associated pressure versus specific volume (reciprocal of the density) plot (i.e., pressure increases at a higher and higher rate as the specific volume decreases); while (b) the anomalous materials must possess a downward curvature in the associated pressure versus specific volume plot.

2.3.1 Air Material Model. *Equation of State.* Air, which is used to fill the Eulerian sub domain, is treated as an ideal gas and, consequently, its equation of state was defined by the ideal-gas gamma-law relation as (Ref 22):

$$P = -P_a + (\gamma - 1)\frac{\rho}{\rho_0}E \qquad \text{(Eq 1)}$$

where P is the pressure (or more precisely over-pressure relative to the ambient pressure, P_a = 1 atm = 101.3 kPa), γ (= 1.4 for a diatomic gas like air) the constant-pressure C_p to constant-volume C_v = 717.6 (J/kg K) specific heat ratio, ρ_0 (= 1.225 kg/m^3) is the ambient-pressure (1 atm) air mass density, ρ is the current mass density and E is the volumetric energy density. Equation 1 is obtained from the standard form of the ideal-gas law through the use of the following two additional relations: $R = C_p - C_v$ and $E = C_v(T - T_0)/\rho_0$, where R is the air-specific gas constant while T and T_0 = 298 K are, respectively, the current and the reference temperatures. Examination of Eq 1 reveals that the total pressure $P + P_a$ scales linearly with ρ (i.e., with the reciprocal of the specific volume) and, hence, air behaves as a normal, shock-supporting material under (compressive) blast-loading conditions.

Strength Model. Since air is a gaseous material, it has no ability to support shear stresses and, hence, no strength model had to be defined for this material.

2.3.2 Kevlar/Phenolic-Resin Composite Material Model. *Equation of State.* In accordance with the work presented in Ref 23, Kevlar/Phenolic-resin composite material is treated as an orthotropic material with material non-linearity's appearing in the hydrostatic (pressure-dependent) part of the stress tensor. Within the orthotropic equation of state used, pressure is defined as:

$$P = -K_1 e_{vol} + K_2 e_{vol}^2 - \frac{1}{3}(C_{11} + C_{21} + C_{31})e_{11}^d - \frac{1}{3}(C_{12} + C_{22} + C_{32})e_{22}^d - \frac{1}{3}(C_{13} + C_{23} + C_{33})e_{33}^d \qquad \text{(Eq 2)}$$

where $K_1 = \frac{1}{9}(C_{11} + C_{22} + C_{33} + 2(C_{12} + C_{23} + C_{31}))$ is the effective bulk modulus, e_{vol} (scales linearly with $(\rho_0/\rho) - 1$) is the volumetric strain, K_2, is a coefficient in the quadratic non-linear correction to the P versus e_{vol} and the last three terms on the right-hand side of Eq 2 represent the contributions of the deviatoric strains, e_{ij}^d, to the pressure. It should be noted that a sum of these contributions is zero in the case of a isotropic linear elastic material.

It should be also noted that the presence of the $K_2 e_{vol}^2$ term in Eq 2 introduces the material volumetric non-linearity. Since K_2 is greater than zero in the case of Kevlar/Phenolic-resin composite, this material behaves as a normal shock-supporting material. Furthermore, due to an expected low extent of energy dissipation, no explicit dependence of pressure on the internal energy density is specified in Eq 1. Values for all the parameters for the Kevlar/Phenolic-resin composite equation of state can be found in our recent work (Ref 17).

Strength Model. As far as the strength model is concerned, it is simply defined by a generalized Hooke's law which uses the orthotropic elastic stiffness matrix to map the deviatoric strain components to the corresponding deviatoric stress components. The components of the elastic stiffness matrix, C_{ij}, appearing in Eq 2 and in the equation for K_1, are defined in terms of the corresponding engineering constants E_{ii}, G_{ij} and ν_{ij} (i,j = 1,2,3) using standard relations. Values for all the parameters for the Kevlar/Phenolic-resin composite strength model can be found in our recent work (Ref 17).

2.3.3 Polyurea Material Model. *Equation of State.* To describe the mechanical response of polyurea under blast loading conditions, the material model reported in Ref 24 was used. Within this model, the hydrostatic response of the material is considered to be elastic while provisions are made for large deformations/motions of the material. Consequently, pressure is defined as:

$$P = -K(T)\frac{\ln(J)}{J}; \qquad K(T) = K(T_{ref}) + m(T - T_{ref}) \qquad \text{(Eq 3)}$$

where subscript ref is used to denote a quantity at the reference temperature, K is the bulk modulus, T is the temperature, m a material parameter, and J (= det(F)) with the deformation gradient F being a quantity which maps the original/reference material configuration into the current/deformed material configuration and det denoting the determinant operator. Since ln(J) represents the (logarithmic strain)

volumetric strain and J decreases during compression, the effective bulk modulus $\frac{K(T)}{J}$ increases with an increase in volumetric compression. Thus, polyurea also behaves as a normal shock-supporting material. Values of all the parameters for the polyurea equation of state can be found in our recent work (Ref 17).

Strength Model. Within the polyurea material model reported in Ref 24, deviatoric response of the material is assumed to be time-dependent and is treated using a geometrically nonlinear, materially linear visco-elastic formulation. To account for the aforementioned time-dependent character of the material deviatoric response, evaluation of the deviatoric stress, σ', at the current time t has to take into consideration the entire deformation history of a given material point from the onset of loading at $t = 0$ to the current time. Based on the procedure outlined in Ref 24, σ' is defined as:

$$\sigma'(t) = 2G_\infty \frac{T}{T_{\text{ref}}} \int_0^t \left(1 + \sum_{i=1}^{n} p_i \exp\left(\frac{-(\xi(t) - \xi(\tau))}{q_i}\right) D'(\tau) d\tau\right) \quad \text{(Eq 4)}$$

where G_∞ is the "long-term" shear modulus (i.e., the value of the shear modulus after infinitely long relaxation time), n is the number of terms in the Prony series exponential-type relaxation function, p_i and q_i are, respectively, the amplitude and the relaxation time of each Prony series term, ξ is the so-called reduced time and D' is the deviatoric part of the rate-of-deformation tensor, D ($D'_{ij} = D_{ij} - 1/3 * D_{ii}\delta_{ij}$, $i,j = 1,2,3$, δ_{ij} is the Kronecker delta second-order tensor, summation is carried out over the repeated indices and *trace* denotes the *trace* operator). The reduced time is utilized to take into account the effect of temperature and pressure on the relaxation kinetics and is defined as:

$$\xi(t) = \int_0^t \frac{dt}{10^{A(T - C_{\text{TP}}P - T_{\text{ref}})/(B + T - C_{\text{TP}}P - T_{\text{ref}})}} \quad \text{(Eq 5)}$$

where A, B and C_{TP} are material constants. Through application of the reduced-time concept, the response of a material at temperature, T, and pressure, P, over a time period t is assumed to be identical to the response of the same material at the reference temperature and pressure over a time period $\xi(t)$. The rate of deformation tensor, D, is related to the deformation gradient, F, as:

$$D = \text{sym}\left(\dot{F}F^{-1}\right) \quad \text{(Eq 6)}$$

where "sym", the raised dot and superscript "-1", are used to denote, respectively, the symmetric part, the time derivative, and the inverse of a second-order tensor. Values of all the parameters for polyurea strength-model can be found in our recent work (Ref 17).

2.3.4 Skull Material Model. *Equation of State.* Skull is composed of bone material which is characterized by relatively low value of the compressibility and an effectively isotropic character of the material microstructure. Consequently, the hydrostatic part of the skull-material model is represented using a Mie-Gruneisen equation of state with a zero value of the Gruneisen gamma parameter in the form:

$$P = \frac{\rho_0 C_0^2 \left(1 - \frac{\rho_0}{\rho}\right)}{\left[1 - s\left(1 - \frac{\rho_0}{\rho}\right)\right]^2} \quad \text{(Eq 7)}$$

where ρ_0 is the initial/reference density and coefficient C_0 (the sound speed) and s relates the shock speed U_s and the resulting particle velocity, U_p, as:

$$U_s = C_0 + s \cdot U_p \quad \text{(Eq 8)}$$

Equation 7 also referred to as a shock-Hugoniot equation of state, is often used to represent non-linear response (associated with an increase in bulk modulus) of the materials under a high level of compression. Thus, skull material also behaves as a normal, shock supporting material. Values of all the parameters for the skull-material equation of state can be found in our recent work (Ref 17).

Strength Model. Due to the high shear rigidity of skull material and an effectively isotropic character of the material microstructure, the deviatoric response of the skull material is defined as being isotropic, linear elastic. Consequently, this response is completely quantified by a single material parameter, the shear modulus μ. The shear modulus is typically defined in terms of the corresponding Young's modulus E and the Poisson's ratio ν, as $\mu = E/[2(1 + \nu)]$. Values of all the parameters for the skull-material strength model can be found in our recent work (Ref 17).

2.3.5 Cerebrospinal Fluid and Cerebrum Material Models. *Equation of State.* Following the analysis presented in our recent work (Ref 17), the materials constituting the cerebrospinal fluid and cerebrum are assumed to be isotropic (direction-invariant) and homogeneous (spatially uniform) and to behave as elastic (time-invariant, materially nonlinear) materials with respect to their hydrostatic/volumetric response. In accordance with these assumptions/simplifications, the hydrostatic portion of the soft-tissue material model is defined using an initial value of the bulk modulus and one or more parameters defining the type and extent of nonlinearity between the pressure, density, and internal energy density.

Specifically, following Moore et al. (Ref 25), the nonlinear hydrostatic/volumetric elastic response of the CSF and cerebrum materials is modeled using a Tait-type equation of state of the form:

$$P = B\left[\left(\frac{\rho}{\rho_0}\right)^{\Gamma_0 + 1} - 1\right] \quad \text{(Eq 9)}$$

where B and Γ_0 are material-specific parameters. It should be noted that the Tait-type equation of state is often used to model the behavior of fluids subjected to compressive (including the shock-based) loading. Since water is the dominant constituent of the CSF and cerebrum materials, and these materials were subjected to shock loading in the present work, the Tait-type equation of state was deemed an appropriate choice. Due to aforementioned chemical similarity between CSF/cerebrum materials and water, Parameters Γ_0 and B for the CSF and cerebrum materials are set equal to their counterparts in water. A summary of the Tait equation of state parameters ρ_0, B, and Γ_0 for the cerebrospinal fluid and cerebrum materials can be found in our recent work (Ref 17).

Strength Model. The deviatoric response of the CSF and cerebrum materials is generally considered as being time-dependent. However, as suggested by an analysis presented in our recent work (Ref 17), the relaxation times of these materials are at least two orders of magnitude longer than the characteristic times encountered in the present work. Hence, viscoelastic response of these materials is ignored and the materials are assumed to remain in a fully unrelaxed state during a typical shock-loading event. Under these conditions, it appeared justified to treat the materials in question as time-invariant elastic materials. Furthermore, in order to account for potential effects associated with large-deformation/motion induced geometrical and material nonlinearities, a hyper-elastic formulation had to be adopted for the deviatoric response of the materials in question.

Following the analysis carried out in our prior work (Ref 17), a Neo-Hookean hyper-elastic model was selected which defines the deviatoric stress as:

$$\sigma' = J^{-1}F\left[\mu \cdot \left(\log\sqrt{C}\right)^{\text{dev}}\right]F^{\text{T}} \qquad \text{(Eq 11)}$$

where F and J were defined previously, μ is the shear modulus and $C = F^{\text{T}}F$ (is the right Cauchy-Green deformation tensor, and superscript T is used to denote a transpose operator). For simplicity, $\sqrt{C}$ term is replaced with its first-order and second-order linearized forms (Ref 26). A summary of the Neo-Hookean hyper-elastic model parameters for CSF and cerebrum can be found in our recent work (Ref 17).

2.3.6 Ethylene-Vinyl-Acetate (EVA) Foam Material Model. EVA foam material was modeled as a hyperelastic highly compressible elastomeric-foam non-linear material whose behavior is described by the following strain energy function:

$$W = \sum_{i=1}^{N}\frac{2\mu_i}{\alpha_i^2}\left[\lambda_1^{\alpha_i} + \lambda_2^{\alpha_i} + \lambda_3^{\alpha_i} - 3 + \frac{1}{\beta_i}\left((J)^{-\alpha_i\beta_i} - 1\right)\right] \qquad \text{(Eq 12)}$$

where N represents the number of terms in the summation, μ_i, α_i, and β_i are material-dependent parameters, λ_i (i = 1,2,3) are the principal stretches (i.e., eigen values of the right (U) or the left stretch (V) tensors obtained through polar decomposition of the deformation gradient, F) defined as: $\lambda_1 = \text{trace}(U)$, $\lambda_2 = \frac{1}{2}[\text{trace}^2(U) - \text{trace}(U^2)]$ and $\lambda_3 = \det(U)$ and $J = \lambda_1\lambda_2\lambda_3 = \det(F)$. In the present case, $N = 2.0$ was used. It should be noted that both terms on the right-hand side of Eq 12 are affected by volumetric (J-dependent) effects, i.e., the deviatoric and volumetric terms are inter-dependent. This can be shown by casting Eq 12 as:

$$W = \sum_{i=1}^{N}\frac{2\mu_i}{\alpha_i^2}\left[J^{-\frac{1}{3}\alpha_i}\left(\bar{\lambda}_1^{-\alpha_i} + \bar{\lambda}_2^{\alpha_i} + \bar{\lambda}_3^{\alpha_i} - 3\right) + 3\left(J^{-\frac{1}{3}\alpha_i} - 1\right) + \frac{1}{\beta_i}\left((J)^{-\alpha_i\beta_i} - 1\right)\right] \qquad \text{(Eq 13)}$$

in which $\bar{\lambda}_i = J^{-1/3}\lambda_i$ and λ_i (i = 1,2,3) are stretches associated with the deviatoric part of deformation alone. Stress (more precisely, the second Piola-Kirchhoff stress tensor, S) is obtained by differentiating the strain energy function U with respect to the right Cauchy-Green deformation tensor, C (= $0.5(F^{\text{T}}F - I)$, I = second-order identity tensor), as:

$$S = 2\frac{\partial W}{\partial C} = 2\frac{\partial W}{\partial \lambda_k}\frac{\partial \lambda_k}{\partial C} \qquad \text{(Eq 14)}$$

The term $\frac{\partial W}{\partial \lambda_k}$ is obtained by properly differentiating Eq 12, the second term is defined by the well-known relations between the eigen values and the components of a second-order tensor while summation over repeated indices is implied in Eq 14. The (true) Cauchy stress, σ, can then be computed from the corresponding second Piola-Kirchoff stress, S, using the following relation:

$$\sigma = J^{-1}FSF^{\text{T}} \qquad \text{(Eq 15)}$$

Since EVA foam becomes volumetrically stiffer as it is compressed, this material behaves as a normal shock-supporting material. A summary of the EVA foam material model parameters can be found in our recent work (Ref 17).

Equation of State. The EVA-foam material model presented above defines the complete stress tensor. Hence, it is not necessary to partition this stress into its hydrostatic and deviatoric components. However, in cases in which the commercial software expects separate definitions of the EOS and the strength model, one can readily derive a hydrostatic-stress function (and, in turn, pressure) from the total-stress function.

Strength Model. If required, the deviatoric stress can be defined as a difference between the total stress and the hydrostatic stress.

2.3.7 Skin/Fat-Tissue Material Model. The skin (as well as the companion muscle tissue) is treated as a single material and modeled using a Mooney-Rivlin hyperelastic isotropic material model which is defined by the following strain energy function:

$$W = A_1(I_1 - 3) + A_2(I_2 - 3) + A_3\left(I_3^{-2} - 1\right) + A_4(I_3 - 1)^2 \qquad \text{(Eq 16)}$$

In Eq 16, the material-dependent parameters A_3 and A_4 are related to the other two parameters, A_1 and A_2, as:

$$A_3 = \frac{1}{2}A_1 + A_2 \qquad \text{(Eq 17)}$$

and

$$A_4 = \frac{A_1(5\nu - 2) + A_2(11\nu - 5)}{2(1 - 2\nu)} \qquad \text{(Eq 18)}$$

To obtain the components of the Cauchy stress, an analogous procedure to that described in the EVA foam material model case is used. Since skin/fat material becomes volumetrically stiffer as it is compressed, this material also behaves as a normal shock-supporting material. A summary of the skin/fat material model parameters can be found in our prior work (Ref 27).

Equation of State. As in the EVA-foam material model case presented above, when required, a hydrostatic-stress function (and, in turn, pressure) can be derived from the total-stress function obtained using the procedure described above.

Strength Model. If required, the deviatoric stress can be defined as a difference between the total stress and the hydrostatic stress.

2.4 Problem Formulation

Interactions between an airborne blast wave and the ACH/head assembly was analyzed in the following way: (a) the initial pressure in Eulerian-domain is set to the atmospheric level; (b) an Eulerian "in-flow" face, which is parallel to the *x*-*y* plane and adjacent to the left-hand side of the ACH/head assembly (from the perspective of the blast subject), is defined to enable influx of air-material associated with the blast wave wake. A time-dependent pressure impulse is next prescribed over this face in accordance with the bi-phasic Friedlander pressure versus time function (Fig. 6). Parameter identification for this function was carried out using the blast simulation code, ConWep, developed by the US Army Corps of Engineers (Ref 28). Details regarding the bi-phasic Friedlander pressure-dependent function and physical character of its parameters can be found in our previous work (Ref 17) and in Ref 29.

In accordance with the prevailing opinion that blast overpressures on the order of 1 atm are important from the mTBI point of view (lower overpressures are of less concern while higher overpressures lead to more severe forms of TBI or death), all the calculations carried out in the present work involved a planar blast wave with 1 atm peak overpressure. As a result of the time-varying pressure application over the in-flow face, a blast wave enters the Eulerian-domain and propagates towards the air/ACH contact surface. Upon reflection of the blast wave from this contact surface, the reflected wave propagates in the opposite direction and ultimately exits the Eulerian-domain; (c) "Out-flow" boundary conditions are applied over the Eulerian-domain face parallel with the in-flow face; and (d) sliding "no-flow" boundary conditions were applied over the remaining Eulerian domain faces.

As far as the boundary conditions are concerned, the following two types were applied simultaneously: (a) to mimic the skull/spine pivot joint; a coupling is created using a set of nodes at the skull base and the associated reference node is kinematically constrained to form a revolute joint; and (b) to mimic the effect of neck-support muscles; six axial-type connectors are placed between four couplings on the skull and the base of the neck (modeled as a set of four nodes fixed in space). Using the approach outlined in our prior work (Ref 27), muscles are modeled as passive elastic elements and their elastic stiffness is set accordingly.

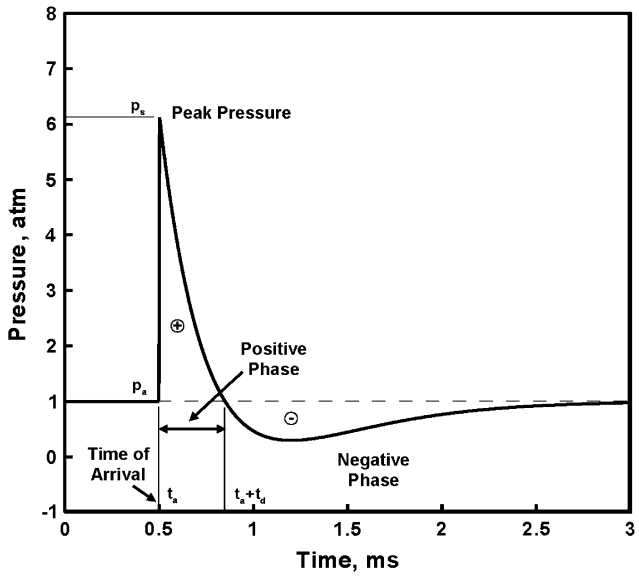

Fig. 6 A typical free-air pressure vs. time relation at a fixed point as defined by the biphasic Friendlander equation

3. Results and Discussion

3.1 Typical Results

In this section, examples are given of the typical results obtained in the present work. In accordance with the radiological convention, only blast-impact over the right (from the perspective of an observer facing the blast-subject) temporal region of the skull was considered. Since the present work involves blast-impact simulations for the unprotected and either standard ACH or augmented ACH, the results in the remainder of this section will be presented accordingly.

3.1.1 Unprotected Head Case. An example of the temporal evolution of the (over)pressure and its spatial distribution over the mid-coronal section in both the Eulerian and the Lagrangian domains for the case of an unprotected head is displayed in Fig. 7(a)-(d). It is seen that the airborne blast wave propagates from the right side and, upon impacting the head, produces a shock pressure wave at the impacted head side. As expected, the shock pressure wave is seen to travel at a higher speed through the head (except perhaps through the skin) than the blast wave does through the air. Consequently, by the time the airborne blast wave reaches the left-hand side of the head, the shock wave within the head has undergone several reflections from the brain/skull, skull/skin, and skin/air interfaces. Also, it can be observed that, as the shock wave propagates through the brain and undergoes multiple reflections, it undergoes attenuation and dispersion/decomposition.

Spatial distributions of the maximum principal normal stress over the mid-coronal ($x = 0$) section of the head at four different simulation times (0.24, 0.26, 0.28, and 0.52 ms) are displayed in Fig. 8(a)-(d). The maximum principal (tensile) stress limits in Fig. 8(a)-(d) are 0 and 600 kPa. It should be noted that in Fig. 8(a)-(d) (as well as in the subsequent hydrodynamic-quantity field figures), the impacted right-hand side of the head is located on the right-hand side of the figure while arrows are used to indicate the direction of motion of the strongest shock wave (at a given simulation time) within the intracranial cavity. A brief examination of the results displayed in Fig. 8(a)-(d) reveals that:

(a) Initial distribution of the maximum principal (tensile) stress (within the intracranial cavity) is controlled by the shock wave transfer from the ambient air to the skin, the skull and, in turn, to the intracranial matter. Subsequent evolution of this stress component, on the other hand, appears to be primarily controlled by the multiple, complex shock wave reflections (at the material boundaries) and interactions (between different intracranial shock waves);
(b) The absolute highest values of the maximum principal (tensile) stresses are about 600 kPa and they are found at a few dynamically changing locations in the intracranial cavity. On the other hand, the maximum levels of this quantity, spread over a larger domain of the brain

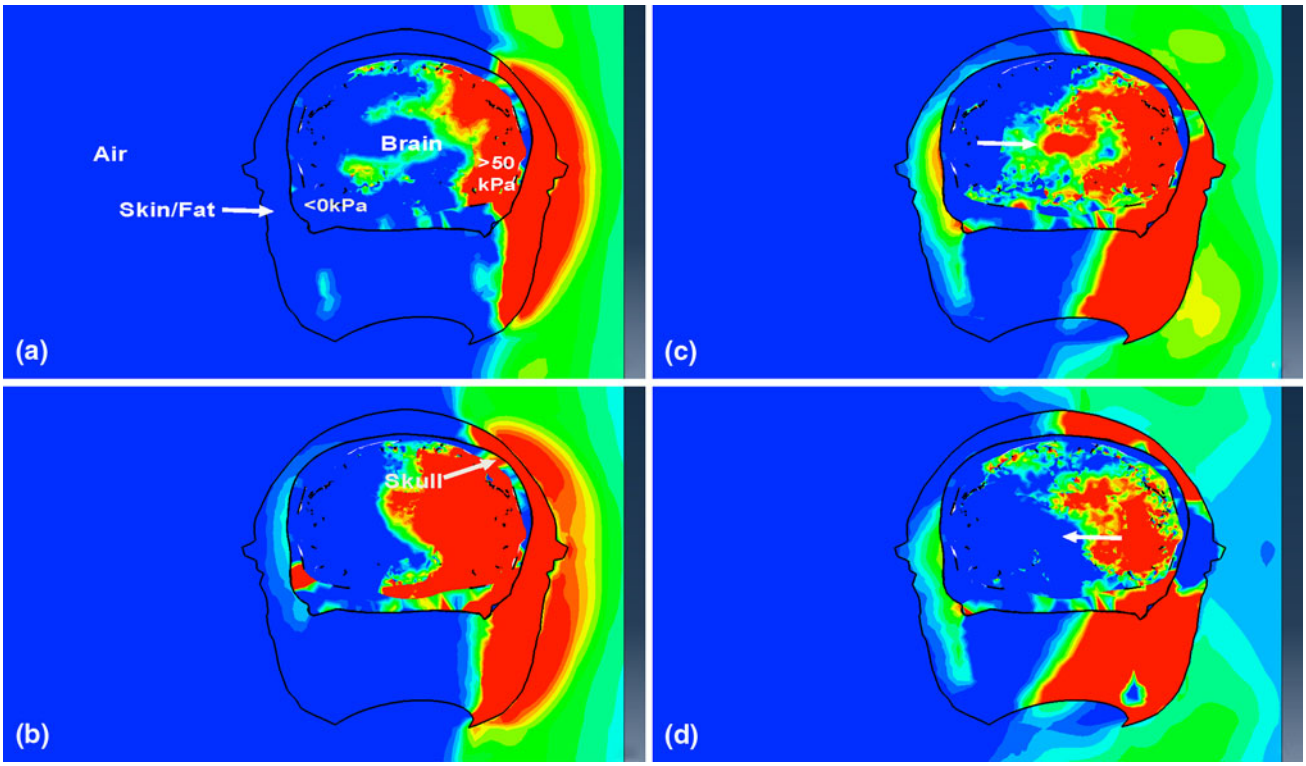

Fig. 7 An example of the temporal evolution of the (over)pressure and its spatial distribution over the mid-coronal section in both the (air) Eulerian and the (skull/brain) Lagrangian domains. Post-impact times: (a) 0.20 ms; (b) 0.25 ms; (c) 0.35 ms; and (d) 0.42 ms

(at the side of the brain opposite to the one impacted by the blast wave, i.e., the so-called "contracoup" side), are around 125 kPa suggesting a 25% increase relative to the incident blast overpressure;

(c) There are some indications that high intracranial principal stress values at the contracoup side are caused by the reflection of the intra-skull compressive shock waves at the skull/skin interface which causes the formation of decompression/tension waves;

(d) It should be noted that the intracranial wave front is generally parallel to the incident blast wave;

(e) The highest values of the maximum principal stress are found in the skull which was expected considering the fact that the associated material is substantially stiffer than the materials found in the skin and the intracranial cavity;

Spatial distributions of the maximum shear stress over the mid-coronal ($x = 0$) section of the head at four different simulation times (0.35, 0.44, 0.46, and 0.48 ms) are displayed in Fig. 9(a)-(d). The (absolute value of the) maximum shear stress in Fig. 9(a)-(d) is 60 kPa and they are found at a few dynamically changing locations in the intracranial cavity. On the other hand, the maximum levels of this quantity, spread over a larger domain of the brain are around 5 kPa. A brief examination of the results displayed in Fig. 9(a)-(d) reveals that:

(a) Unlike the case of the maximum principal stress, initial distribution of the maximum shear stress does not appear to be controlled by the transfer of the incident blast wave into the skin/skull/brain assembly. Rather, the incident blast wave induces shear stresses in the skull. However, only a minute fraction of these stresses are transferred into the intracranial cavity due to the fluid-like, low shear stiffness, inviscid character of the CSF material. Careful examination of the temporal evolution of shear stresses within the intracranial cavity revealed that they are primarily the result of multiple, complex reflections, and interactions of the intracranial compressive/tensile shock wave(s);

(b) Intracranial shear stress level(s) (ca. 5 kPa) are substantially lower (ca. 1-2 orders of magnitude) than their principal stress level(s) counterpart(s) (ca. 125 kPa). As stated above, this finding is consistent with the fact that the brain is fairly shear-compliant and that it is separated from the skull by a layer of nearly inviscid and highly shear-compliant CSF;

(c) In sharp contrast to the maximum principal stresses which tend to level off in the later stages of the simulation, the maximum shear stresses continue to build over the full simulation time;

(d) Statistically, very high levels of the maximum shear stress in the brain are observed within the brain stem, Fig. 9(d), and this finding appears to be related to the fact that the brainstem material possesses the highest shear stiffness among the intracranial materials; and

(e) The peak values of the maximum shear stress in the head are observed within the skull, Fig. 9(a)-(d), and this finding is related to the fact that the skull material possesses the highest shear stiffness among the head materials.

3.1.2 ACH-Protected Head Case. In the case of the ACH-protected head, qualitatively similar results for the spatial distribution and temporal evolution of the (over)pressure are

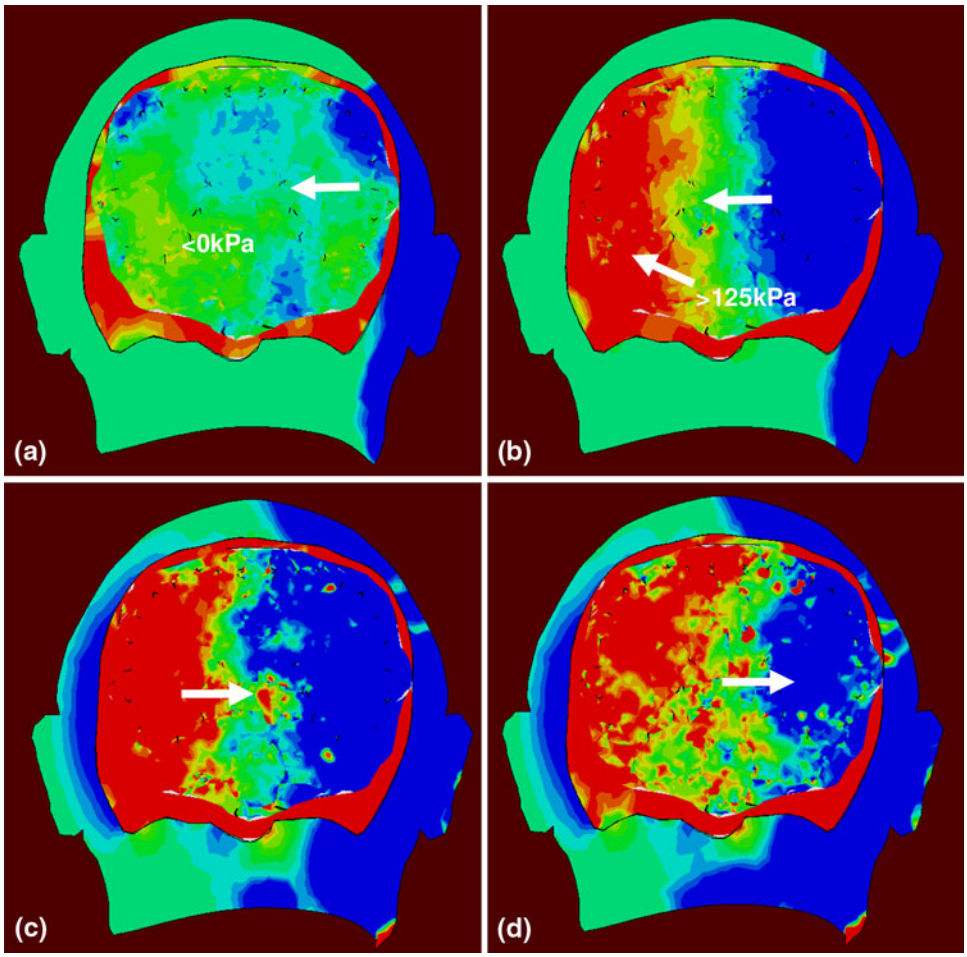

Fig. 8 Spatial distribution of the maximum principal stress over the mid-coronal section of the head, for the unprotected head case, at four post-blast-impact times: (a) 0.24 ms; (b) 0.26 ms; (c) 0.28 ms; (d) 0.52 ms. Principal stress range (0.0 kPa, 125 kPa)

obtained as those depicted in Fig. 7(a)-(d) (for the unprotected head case). These results are not shown for brevity but they clearly revealed the shock-mitigation role of the ACH since the pressure levels in the intracranial cavity were reduced on average by ca. 50%.

Spatial distributions of the maximum principal stress over the mid-coronal ($x = 0$) plane at four different post-blast times (0.27, 0.33, 0.45, and 0.54 ms) for the standard configuration ACH-protected head case are displayed in Fig. 10(a)-(d). Similar qualitative results are obtained in the case of augmented ACH-protected head but are not shown for brevity.

The maximum principal stress limits in Fig. 10(a)-(d) are −60 and 60 kPa. A brief examination of the results displayed in Fig. 10(a)-(d) and their comparison with the results displayed in Fig. 8(a)-(d) reveals that:

(a) The ACH standard configuration provides a substantial blast mitigation role since the maximum principal intracranial stresses in Fig. 10(a)-(d) are on average lower by ca. 40-50% than their unprotected head counterparts displayed in Fig. 8(a)-(d);
(b) Additional qualitative evidence for blast protection offered by the helmet is apparent since the ingress of the blast wave takes place mainly through the exposed portion of the head. Consequently, the wave front of the intracranial shock wave is no longer parallel to the incident blast wave. In other words, there is a vertical component of the intracranial shock wave. This finding is quite significant and suggests that to minimize the danger of blast-induced TBI, no portion of the head should be left unprotected. For example, the face portion of the head should be protected by a visor while the neck should be protected by a nape pad; and
(c) Same findings, as in the unprotected head case, were obtained regarding the origination of intracranial shocks, their interactions and the role of skull shock reflection at the contracoup skull/skin interface.

Spatial distributions of the maximum shear stress over the mid-coronal ($x = 0$) plane at four different post-blast times (0.35, 0.44, 0.49, and 0.56 ms) for the standard configuration ACH-protected head case are displayed in Fig. 11(a)-(d). Similar qualitative results are obtained in the case of augmented ACH-protected head but are also not shown for brevity.

The maximum shear stress limits in Fig. 11(a)-(d) are 0 and 2.3 kPa. A brief examination of the results displayed in Fig. 11(a)-(d) and their comparison with the results displayed in Fig. 9(a)-(d) reveals that:

(a) The ACH standard configuration provides a substantial blast mitigation role since the maximum shear intracranial stresses in Fig. 11(a)-(d) are on average lower by

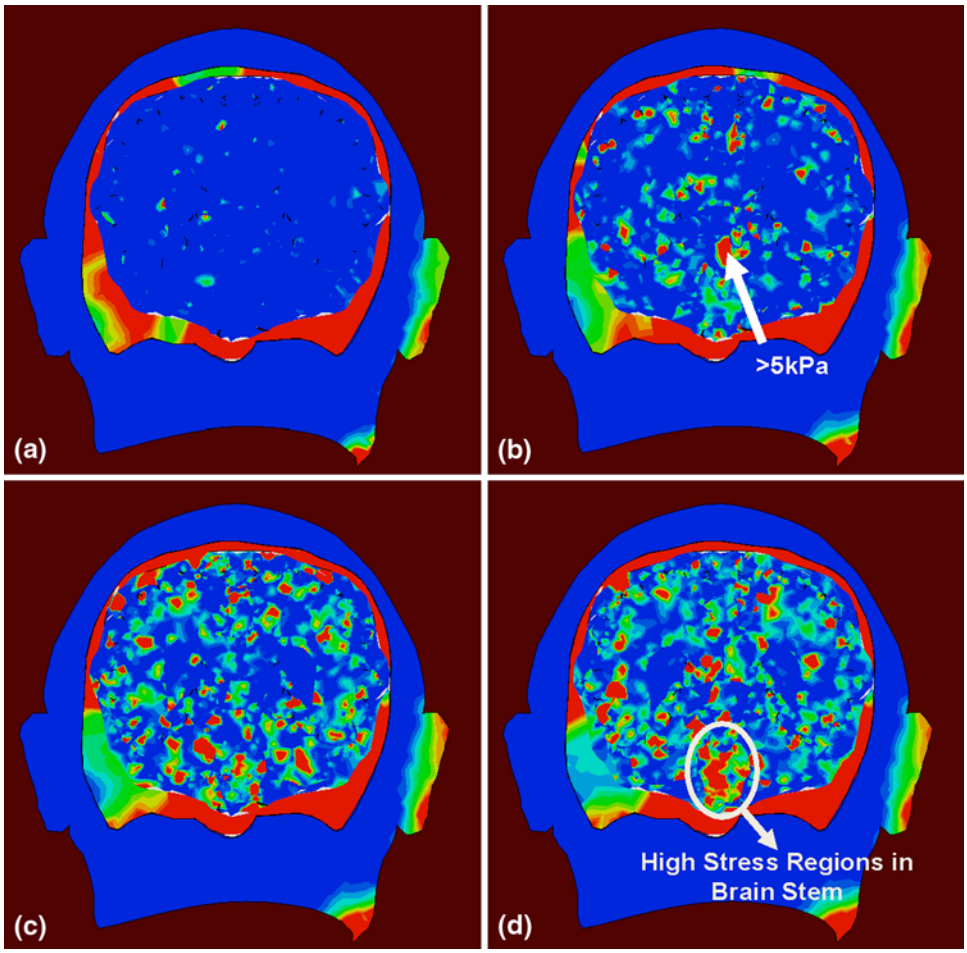

Fig. 9 Spatial distribution of the maximum shear stress over the mid-coronal section of the head, for the unprotected head case, at four post-blast-impact times: (a) 0.35 ms; (b) 0.44 ms; (c) 0.46 ms; (d) 0.48 ms. Shear stress range (0.0 kPa, 5 kPa)

over 50% than their unprotected head counterparts displayed in Fig. 9(a)-(d);

(b) Similar findings as in the case of the protected head maximum principal stress case regarding the ingress of the blast wave and the orientation of the intracranial shock front are observed here;

(c) Figure 11(c) and (d) shows some evidence for the ingress of shear stresses into the intracranial cavity through the suspension pads; and

(d) Same findings, as in the unprotected head case, were obtained regarding the origination of intracranial shear waves and their interactions as well as regarding the presence of peak shear stresses within the brainstem.

3.2 Identification of mTBI-Causing Mechanical Quantities

Before the shock-mitigation efficacy of the ACH and its different augmentations could be quantified, mechanical quantities which are most likely responsible for mTBI have to be first identified. As mentioned earlier, the three most common types of non-penetrating mTBIs are: (a) diffuse axonal injury; (b) contusion; and (c) subdural hemorrhage. A brief description of each of these mTBIs is given below along with the identification of the associated injury-causing mechanical quantities. To help the reader relate to the most probable locations of the three types of mTBI, a surface-topology and a median sagittal section brain map are provided in Fig. 12(a) and (b), respectively (Ref 30).

3.2.1 Diffuse Axonal Injury. Diffuse axonal injuries are believed to be caused by blast-induced stretching and shearing of axons and small vessels which, in turn, lead to impaired axonal transport and subsequent focal axonal swelling and eventual disconnection (Ref 6). The most common locations for this type of mTBI are the corticomedullary (gray matter-white matter) junction (particularly in the frontal and temporal areas), internal capsule, deep gray matter, upper brainstem, and the corpus callosum (Ref 6). Based on this description of the diffuse axonal injury, maximum principal (tensile) stress, and maximum shear stress within the intracranial cavity are identified as most probable mechanical causes for this type of mTBI.

3.2.2 Contusion. Contusion occurs when the brain undergoes a sufficiently large relative motion with respect to the skull resulting in brain/skull collision. This typically leads to bruising of the brain parenchyma (functional parts of the brain tissue), as well as hemorrhage (bleeding) and edema (fluid accumulation). The most common locations for this type of mTBI are the superficial gray matter of the inferior, lateral, and anterior aspects of the frontal and temporal lobes, with the occipital poles or cerebellum less often involved (Ref 6). Based on the above description of this type of mTBI, the most appropriate injury-causing mechanical quantity would be the intensity of

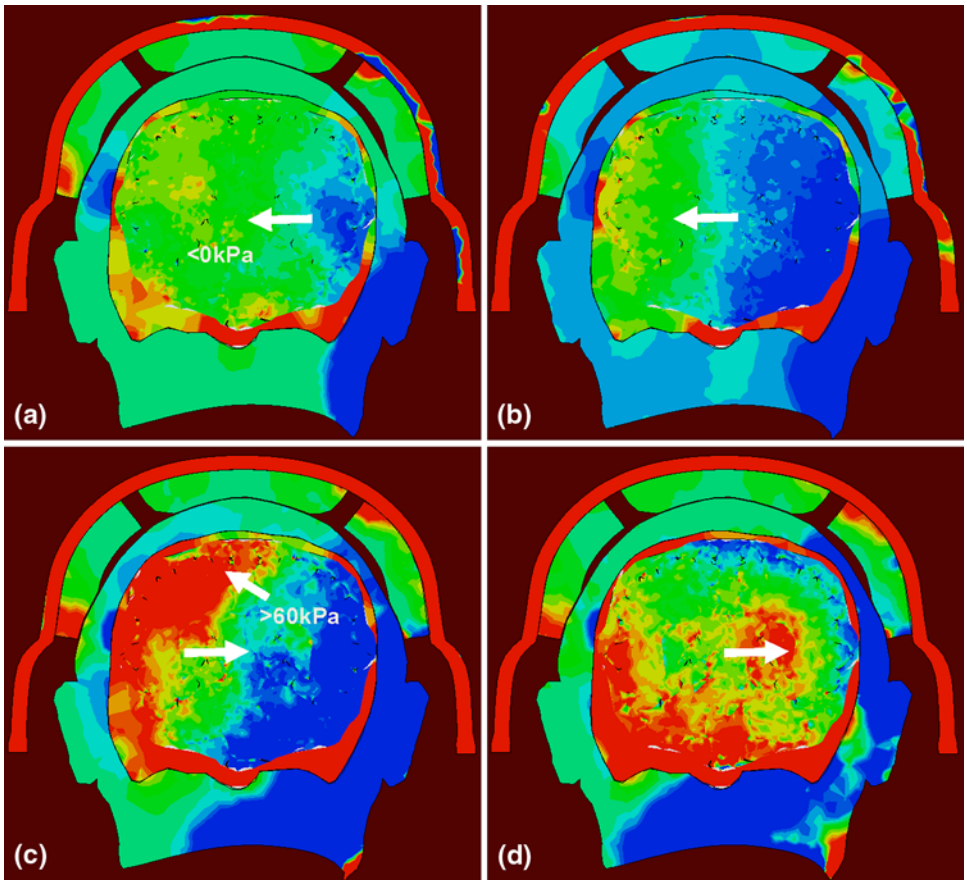

Fig. 10 Spatial distribution of the maximum principal stress over the mid-coronal section of the head, for the protected head case, at four simulation times: (a) 0.27 ms; (b) 0.33 ms; (c) 0.45 ms; (d) 0.54 ms. Maximum principal stress range (−80 kPa, 80 kPa)

brain/skull collision. However, no direct evidence of such collision was obtained in the present work for the following two reasons: (a) prohibitively long simulation times would have been needed; and (b) due to the fact that CSF was modeled as a Lagrangian part in the present work (and no deletion option was used), direct brain/skull contact was not possible. To overcome this problem, reduction in the CSF local thickness has been used as a measure of the probability for brain/skull collision.

3.2.3 Subdural Hemorrhage. Subdural hemorrhage occurs when the surface layers of the brain experience severe distortions due to the ingress of blast wave induced shear stresses resulting in tearing of the tributary surface veins which connect the brain surface and the dural venous sinus (a vein hub which returns blood and cerebrospinal fluid to the jugular vein). Due to the viscoelastic dissipative nature of the brain tissue material, shear stresses and distortions are highest in the frontal and parietal brain surface regions adjacent to the location of blast wave ingress (Ref 6). In line with these observations, maximum shear stress over the surface of the brain lobes was identified as the appropriate injury-causing mechanical quantity.

3.3 Shock-Mitigation Efficacy of Different ACH Augmentations

In this section, the mechanical quantities identified in the previous section are assessed for the following five air/ACH/head cases: (a) Case A: unprotected head; (b) Case B: standard ACH-protected head; (c) Case C: ACH-protected head with polyurea suspension pads; (d) Case D: Standard ACH-protected head with polyurea internal lining; and (e) Case E: Standard ACH-protected head with polyurea external coating. These assessments are then used to judge the shock-mitigation efficacy of the standard ACH and its three augmentations. In the remainder of this section, the pertinent results are presented for each of the three types of mTBI.

3.3.1 Diffuse Axonal Injury. As discussed earlier, the mechanical quantities believed to be most responsible for this type of mTBI are the maximum tensile stress and the maximum shear stress experienced by the white matter regions of the brain. Peak values of the maximum tensile stress and the maximum shear stress obtained in the present work are, respectively, shown in Fig. 13(a) and (b), for the aforementioned five air/helmet/head configurations. Examination yielded the following findings:

(a) A comparison of cases A and B shows that the standard ACH case significantly reduces the probability and severity of blast-induced diffuse axonal injury, since the peak maximum tensile and shear stresses are reduced by ~40-50%. However, it should be recalled that in general, the ACH in its standard configuration is not considered as providing adequate protection against this type of injury. Hence, for the ACH alteration to be considered as effective, they must substantially reduce the peak tensile and shear stress levels below those found in the standard ACH case;

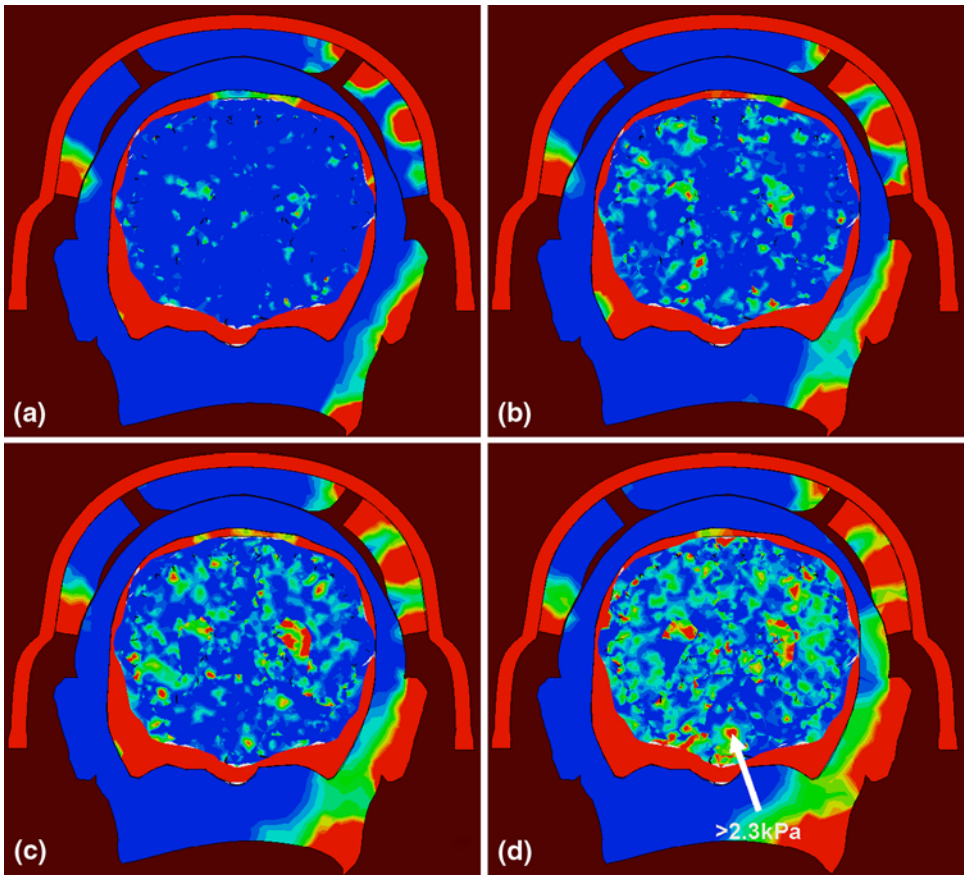

Fig. 11 Spatial distribution of the maximum shear stress over the mid-coronal section of the head, for the protected head case, at four simulation times: (a) 0.35 ms; (b) 0.44 ms; (c) 0.49 ms; and (d) 0.56 ms. Shear stress range (0.0 kPa, 2.3 kPa)

(b) Replacement of the EVA suspension pads (Case B) with the polyurea pads (Case C) has an adverse effect, since the resulting peak maximum tensile stress and peak maximum shear stress are higher in Case C by ~30 and ~10%, respectively;
(c) Addition of a 2-mm-thick polyurea internal lining (Case D) to the standard ACH design (Case B) offers only a minimal shock-mitigation benefit since the accompanying reductions in peak maximum tensile stress and peak maximum shear stress are ~2 and ~6%, respectively;
(d) Addition of a 2-mm-thick polyurea external coating (Case E) to the standard ACH design (Case B) also only offers only a minimal shock-mitigation benefit since the accompanying reductions in peak maximum tensile stress and peak maximum shear stress are ~1 and ~8%, respectively; and
(e) Among the four ACH configurations, the two which yield the lowest probability for diffuse axonal injury are those containing additions of a polyurea internal lining (Case D) and external coating (Case E).

3.3.2 Contusion. As discussed earlier, the mechanical quantity used to judge the probability for contusion is the extent of CSF thickness reduction. Peak values of the CSF thickness reduction for the aforementioned five air/helmet/head configurations are shown in Fig. 14. Examination of the results displayed in this figure reveals that:

(a) A comparison of cases A and B shows that the standard ACH case significantly reduces the probability and severity of blast-induced diffuse axonal injury, since the peak CSF thickness reduction decreases by ~50%. However, as in the case of diffuse axonal injury, the current ACH is generally believed to be ineffective in blast mitigation and only an ACH alteration leading to a substantial decrease in peak CSF thickness reduction from the current ACH configuration could be considered to provide adequate protection against this type of injury;
(b) Replacement of the EVA suspension pads (Case B) with the polyurea pads (Case C) has a severe adverse effect, since the peak CSF thickness reduction increases by nearly 200%. It appears that polyurea pads act as high shock-impedance wave guides which provide a more direct ingress of shock waves generated within the helmet shell into the head;
(c) Addition of a 2-mm-thick polyurea internal lining (Case D) to the standard ACH design (Case B) offers a marginal shock-mitigation benefit since the peak CSF thickness reduction decreases by ~10%;
(d) Addition of a 2-mm-thick polyurea external coating (Case E) to the standard ACH design (Case B) slightly adversely affects the ACH, as the peak CSF thickness reduction increases by ~10%; and
(e) Among the four ACH configurations, the one which yields the lowest probability for contusion is the case

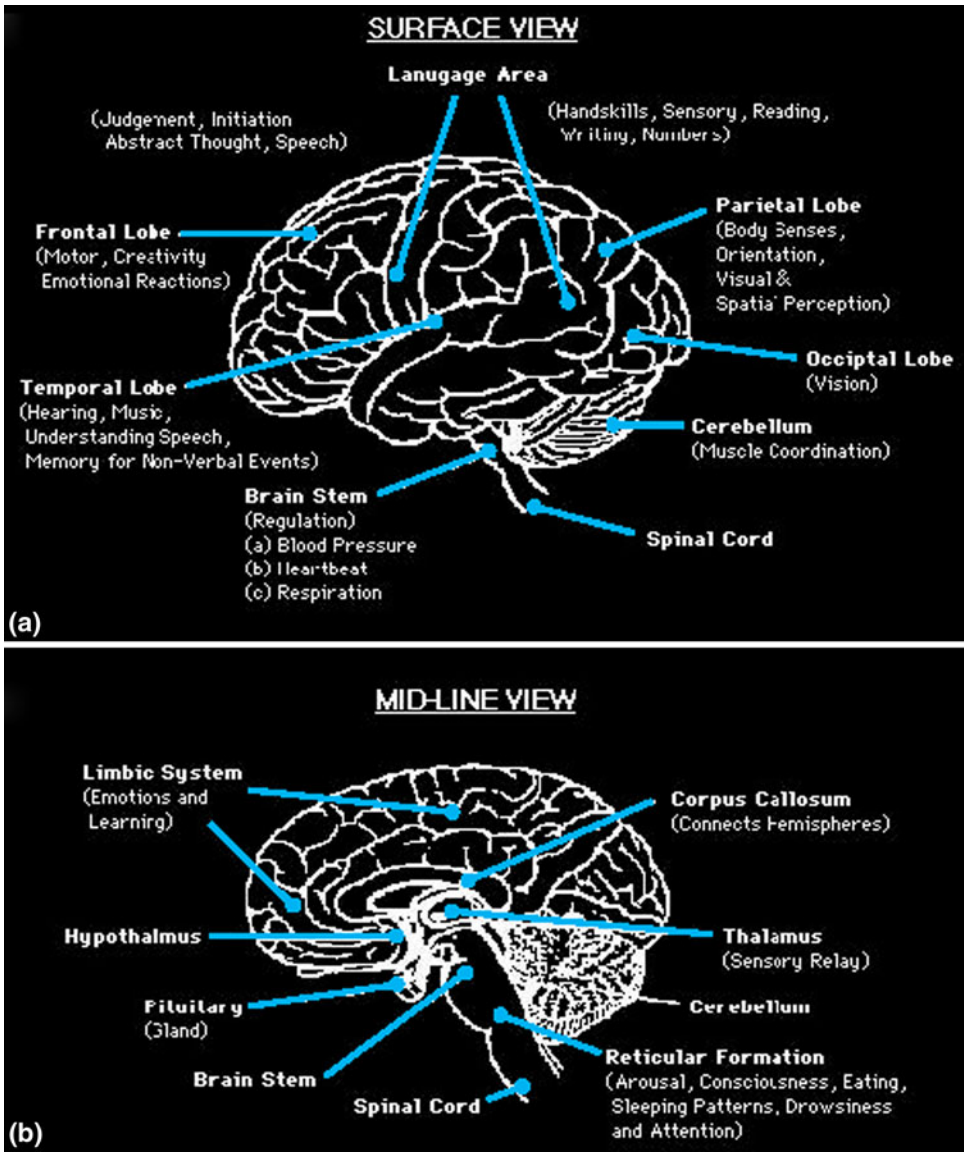

Fig. 12 A simple schematic of the brain map (Ref 30): (a) surface topology; and (b) a median sagittal section

involving an addition of a polyurea internal lining (Case D).

3.3.3 Subdural Hemorrhage. As discussed earlier, the mechanical quantity believed to be most responsible for this type of mTBI is the maximum shear stress experienced by the surface of the brain lobes. Peak values of the brain-surface shear stress for the aforementioned five air/helmet/head configurations are shown in Fig. 15. Examination of the results displayed in this figure reveals that:

(a) A comparison of cases A and B shows that the standard ACH case significantly reduces the probability and severity of blast-induced subdural hemorrhage, since the peak brain-surface shear stress is reduced by ~40%. However, as in the case of diffuse axonal injury and contusion, the current ACH is generally believed to be ineffective in blast mitigation and only an ACH alteration leading to a substantial decrease in peak brain-surface shear stress from the current ACH configuration could be considered to provide adequate protection against this type of injury;
(b) Replacement of the EVA suspension pads (Case B) with the polyurea pads (Case C) has an adverse effect, since the resulting peak brain-surface shear stress is higher in Case C by ~70%;
(c) Addition of a 2-mm-thick polyurea internal lining (Case D) to the standard ACH design (Case B) offers only a minimal shock-mitigation benefit since the accompanying reduction in peak brain-surface shear stress is ~6%;
(d) Addition of a 2-mm-thick polyurea external coating (Case E) to the standard ACH design (Case B) also only offers only a minimal shock-mitigation benefit since the accompanying reduction in peak brain-surface shear stress is ~3%; and
(e) Among the four ACH configurations, the one which yields the lowest probability for subdural hemorrhage is the case involving an addition of a polyurea internal lining (Case D).

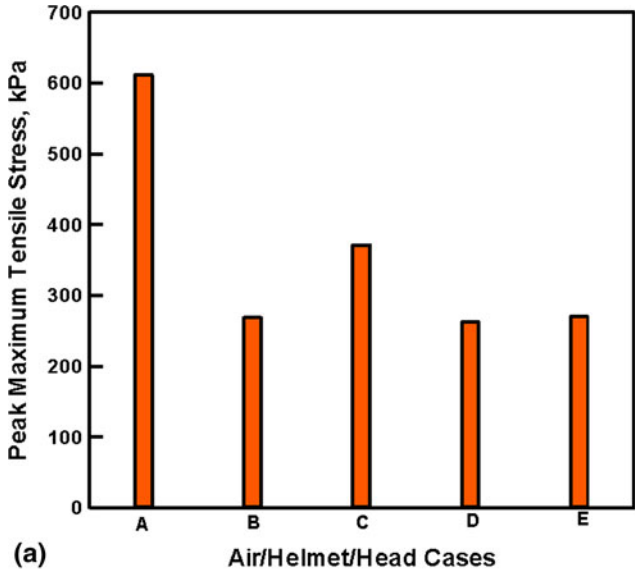

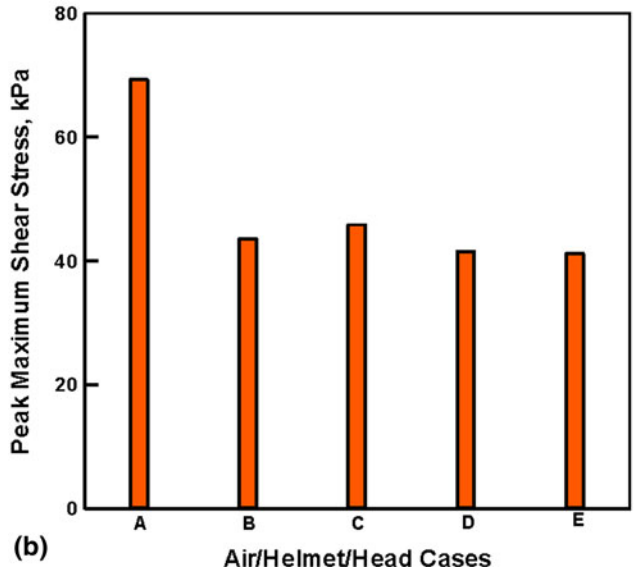

Fig. 13 Peak values of (a) the maximum tensile stress; and (b) the maximum shear stress for the five air/helmet/head configurations

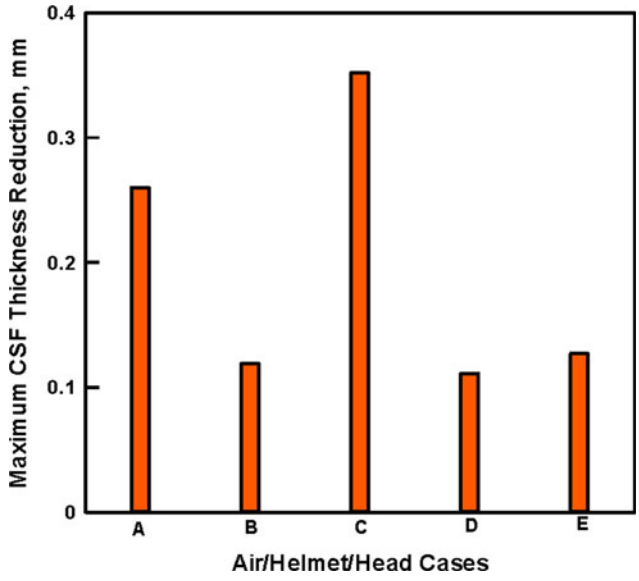

Fig. 14 Peak values of CSF thickness reduction for the five air/helmet/head configurations

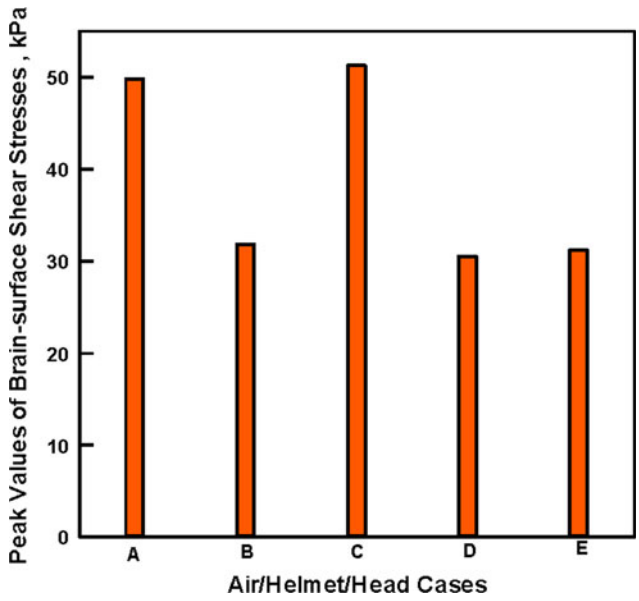

Fig. 15 Peak values of brain-surface shear stresses for the five air/helmet/head configurations

3.3.4 Identification of the Optimal ACH design. The results previously presented in this section reveal that among different polyurea-based modifications of the ACH, only the one associated with the use of a 2-mm-thick polyurea internal lining shows consistent improvements in the protection against all three main forms of mTBI. However, the extent of the shock-mitigation improvements offered by this ACH design variation is relatively small to the overall mitigation capabilities already offered by the standard ACH. This could be understood by both comparing the Case D and Case B results in Fig. 13-15 and Case B and Case A results in the same figures. These two comparisons show that the standard ACH provides substantially more protection relative to the unprotected head case than does the internal lining modified ACH relative to the standard ACH. Based on this finding and the fact that it is generally believed that the standard ACH does not provide adequate blast-induced mTBI protection, one can conclude (even in the absence of well-defined mTBI thresholds) that the investigated ACH augmentations will not render the required level of blast-induced mTBI protection.

4. Summary and Conclusions

Based on the results obtained in the present work, the following main summary remarks and conclusions can be drawn:

(1) Different modifications in the design of the ACH are considered in order to identify those which have a potential for improving the protection offered by the ACH

against different types of blast-induced TBI. All the design modifications considered are based on the use of polyurea-based shock-mitigation structures, as this micro-segregated elastomeric copolymer has shown superior shock-mitigation capabilities. Specific augmentations include replacement of the currently used suspension-pad material with polyurea and the introduction of a thin polyurea internal lining/external coating to the ACH shell.

(2) The investigation carried out in the present work is of a purely computational nature and involved the use of a series of combined Eulerian/Lagrangian transient nonlinear dynamics finite element fluid/solid interaction analyses. The use of these analyses entails construction, parameterization, and validation of detailed constitutive models for a number of structural materials as well as for a number of hard and soft-tissue biological materials.

(3) The efficacy of the modified ACH designs was analyzed by: (a) identifying the main forms of mTBI (axonal damage, contusion, and subdural hemorrhage); (b) establishing the key mechanical causes for these forms of injuries (maximum principal normal and shear stresses and brain/skull collision probability); and (c) quantifying the changes in the magnitude of these mechanical causes brought about by the different ACH design modifications.

(4) The results obtained show that among the ACH variations, the one associated with a 2-mm-thick polyurea internal lining displays the best blast mitigation performance. However, the extent of the additional protection offered by this ACH design variation is relatively small in comparison to that found in the standard ACH design.

Acknowledgments

The material presented in this paper is based on work supported by the Office of Naval Research (ONR) research contract entitled "Elastomeric Polymer-By-Design to Protect the Warfighter Against Traumatic Brain Injury by Diverting the Blast Induced Shock Waves from the Head", Contract Number 4036-CU-ONR-1125 as funded through the Pennsylvania State University. The authors are indebted to Dr. Roshdy Barsoum of ONR for continuing support and interest in the present work and to Professors G. Settles and M. Hargather for stimulating discussions and friendship.

References

1. R. Goel, "Study of an Advanced Helmet Liner Concept to Reduce TBI: Experiments & Simulation Using Sandwich Structures," MS thesis, Massachusetts Institute of Technology, 2011
2. G.A. Christou, "Development of a Helmet Liner for Protection Against Blast Induced Trauma," MS thesis, Massachusetts Institute of Technology, February 2010
3. B.E. Wojcik, C.R. Stein, K. Bagg, R.J. Humphrey, and J. Orosco, Traumatic Brain Injury Hospitalization of U.S. Army Soldiers Deployed to Afghanistan and Iraq, *Am. J. Prev. Med.*, 2010, **38**, p S108–S116
4. D. Warden, Military TBI, during the Iraq and Afghanistan Wars, *J. Head Trauma Rehabil.*, 2006, **21**, p 398–402
5. S. Okie, Traumatic Brain Injury in the War Zone, *N. Engl. J. Med.*, 2005, **352**, p 2043–2047
6. K.H. Taber, D.L. Warden, and R.A. Hurley, Blast-Related Traumatic Brain Injury: What Is Known?, *J. Neuropsychiatry Clin. Neurosci.*, 2006, **18**, p 141–145
7. S.J. Wallsten and K. Kosec, "Social Science Research Network," Paper No. 05-19, 2005, http://ssrn.com/abstract=848408
8. L. Holm, J.D. Cassidy, L.J. Carroll, and J. Berg, Neurotrauma Task Force on Mild Traumatic Brain Injury of the WHO Collaborating Centre: Summary of the WHO Collaborating Centre for Neurotrauma Task Force on Mild Traumatic Brain Injury, *J. Rehabil. Med.*, 2005, **37**, p 131–141
9. I. Cernak, Z. Wang, J. Jiang, X. Bian, and J. Savic, Ultrastructural and Functional Characteristics of Blast Injury-induced Neurotrauma, *J. Trauma*, 2001, **50**, p 695–706
10. M. Grujicic, W.C. Bell, B. Pandurangan, and T. He, Blast Wave Impact-Mitigation Capability of Polyurea When Used as Helmet Suspension Pad Material, *J. Mater. Des.*, 2010, **31**(9), p 4050–4065
11. S.M. Walsh, R.R. Scott, and D.M. Spagnuolo, *The Development of a Hybrid Thermoplastic Ballistic Material with Application to Helmets*, ARL-TR-3700, Army Research Laboratory, December 2005
12. I. Cernak, Z. Wang, J. Jiang, X. Bian, and J. Savic, Ultrastructural and Functional Characteristics of Blast Injury-Induced Neurotrauma, *J. Trauma*, 2001, **50**(4), p 695–706
13. M. Grujicic, G. Arakere, and T. He, Material Modeling and Structural Mechanics Aspects of Traumatic Brain Injury Problem, *Multidiscip. Model. Mater. Struct.*, 2010, doi:10.1108/15736101011080097
14. M. Grujicic, T. He, B. Pandurangan, J. Runt, J. Tarter, and G. Dillon, Development and Parameterization of a Time-Invariant (Equilibrium) Material Model for Segmented Elastomeric Polyureas, *J. Mater. Des. Appl.*, 2011, **225**, doi:10.1177/0954420711401959
15. M. Grujicic, T. He, and B. Pandurangan, Experimental Characterization and Material-Model Development for Microphase-Segregated Polyurea: An Overview, *J. Mater. Eng. Perform.*, 2010, doi:10.1007/s11665-011-9875-6
16. M. Grujicic, B. Pandurangan, A.E. King, J. Runt, J. Tarter, and G. Dillon, Multi-Length Scale Modeling and Analysis of Microstructure Evolution and Mechanical Properties in Polyurea, *J. Mater. Sci.*, 2010, **46**(6), p 1767–1779
17. M. Grujicic, W.C. Bell, B. Pandurangan, and P.S. Glomski, Fluid/Structure Interaction Computational Investigation of the Blast Wave Mitigation Efficacy of the Advanced Combat Helmet, *J. Mater. Eng. Perform.*, 2010, **20**(6), p 877–893
18. M. Grujicic, B. Pandurangan, W.C. Bell, B.A. Cheeseman, C.-F. Yen, and C.L. Randow, Molecular-Level Simulations of Shock Generation and Propagation in Polyurea, *Mater. Sci. Eng. A*, 2011, **528**(10–11), p 3799–3808
19. M. Grujicic, B. Pandurangan, T. He, B.A. Cheeseman, C.-F. Yen, and C.L. Randow, Computational Investigation of Impact Energy Absorption Capability of Polyurea Coatings via Deformation-Induced Glass Transition, *Mater. Sci. Eng. A*, 2010, **527**(29–30), p 7741–7751
20. *ABAQUS*, Version 6.10EF-1, User Documentation, Dassault Systems, Providence, RI, 2010
21. *Hypermesh*, HyperWorks 10.0, Altair Engineering, Inc., Troy, MI, 2010
22. L. Davison, *Fundamentals of Shockwave Propagation in Solids*, Springer-Verlag, Berlin, 2008
23. *ANSYS/Autodyn-2D and 3D*, Version 6.1, User Documentation, ANSYS Inc., 2007
24. A.V. Amirkhizi, J. Isaacs, J. McGee, and S. Nemat-Nasser, An Experimentally-based Viscoelastic Constitutive Model for Polyurea, including Pressure and Temperature Effects, *Philos. Mag.*, 2006, **86**(36), p 5847–5866
25. D.F. Moore, R. Radovitzky, L. Shupenko, A. Klinoff, M.S. Jaffee, and J.M. Rosen, Blast Physics and Central Nervous System Injury, *Future Neurol. Ann. Neurol.*, 2008, **64**, p S30
26. A. Cuitiño and M. Ortiz, A Material-independent Method for Extending Stress Update Algorithms from Small-Strain Plasticity to Finite Plasticity with Multiplicative Kinematics, *Eng. Comput.*, 1992, **9**, p 437–451
27. M. Grujicic, B. Pandurangan, G. Arakere, W.C. Bell, T. He, and X. Xie, Seat-Cushion and Soft-Tissue Material Modeling and a Finite-Element Investigation of Seating Comfort for Passenger Vehicle Occupants, *Mater. Des.*, 2009, **30**, p 4273–4285

28. D. Hyde, *User's Guide for Microcomputer Programs, CONWEP and FUNPRO—Applications of TM 5-855-1*, U.S. Army Engineer Waterways Experimental Station, Vicksburg, 1988
29. P.W. Cooper, *Explosives Engineering*, Wiley-VCH, New York, 1996
30. The Perspectives Network: Survive with Pride, Brain Map, http://www.tbi.org/html/brain_map.html